Article

Highly selective oxidation of ethyl lactate to ethyl pyruvate catalysed by mesoporous vanadia–titania

Wei Zhang, Giada Innocenti, Paula Oulego, Vitaly Gitis, Hai-Hong Wu, Bernd Ensing, Fabrizio Cavani, Gadi Rothenberg, and N. Raveendran Shiju

ACS Catal., **Just Accepted Manuscript** • DOI: 10.1021/acscatal.7b03843 • Publication Date (Web): 09 Jan 2018

Highly selective oxidation of ethyl lactate to ethyl pyruvate catalysed by mesoporous vanadia-titania

Wei Zhang,[a] *Giada Innocenti,*[b] *Paula Oulego,*[c] *Vitaly Gitis,*[d] *Haihong Wu,*[e] *Bernd Ensing*,*[a] *Fabrizio Cavani,*[b] *Gadi Rothenberg* [a] *and N. Raveendran Shiju**[a]

[a] Van 't Hoff Institute for Molecular Sciences, University of Amsterdam, P.O. Box 94157, 1090GD Amsterdam, The Netherlands.

[b] Dipartimento di Chimica Industriale, ALMA MATER STUDIORUM Università di Bologna, Viale Risorgimento 4, 40136 Bologna, Italy.

[c] Department of Chemical and Environmental Engineering, University of Oviedo, C/ Julián Clavería, s/n. E-33071, Oviedo, Spain.

[d] Unit of Environmental Engineering, Ben-Gurion University of the Negev, PO Box 653, Beer-Sheva 84105, Israel.

[e] Shanghai Key Laboratory of Green Chemistry and Chemical Processes, Department of Chemistry, East China Normal University, 3663 North Zhongshan Road, Shanghai, 200062, China.

ABSTRACT: The direct oxidative dehydrogenation of lactates with molecular oxygen is a 'greener' alternative for producing pyruvates. Here we report a one-pot synthesis of mesoporous vanadia-titania (VTN), acting as highly efficient and recyclable catalysts for the conversion of ethyl lactate to ethyl pyruvate. These VTN materials feature high surface areas, large pore volumes and high density of isolated vanadium species, which can expose the active sites and facilitate the mass transport. Compared to homogeneous vanadium complexes and VO_x/TiO_2 prepared by impregnation, the meso-VTN catalysts showed superior activity, selectivity and stability in the aerobic oxidation of ethyl lactate to ethyl pyruvate. We studied also the effect of various vanadium precursors which revealed that the vanadium-induced phase transition of meso-VTN from anatase to rutile depends strongly on the vanadium precursor. NH_4VO_3 was found to be the optimal vanadium precursor, forming more monomeric vanadium species. V^{4+} as the major valence state was incorporated into the lattice of NH_4VO_3 derived VTN material, yielding more V^{4+}–O–Ti bonds in anatase-dominant structure. *In situ* DRIFT spectroscopy and density functional theory calculations show that V^{4+}–O–Ti bonds are responsible for the dissociation of ethyl lactate over VTN catalysts, and for further activating the deprotonation of β-hydrogen. Molecular oxygen can replenish the surface oxygen to regenerate the V^{4+}–O–Ti bonds.

KEYWORDS: biomass conversion • heterogeneous catalysis • mesoporous materials • *in situ* DRIFTS • DFT

INTRODUCTION

Lignocellulosic biomass is attracting increased attention as a renewable carbon source for commodity chemicals.[1] Unlike with fuel applications, the high oxygen content and diversity of biomass-derived 'platform molecules' make them suitable feedstocks for high-added-value chemicals.[2] Lactic acid (LA) and lactates are such platform molecules. They can be converted to several commodity chemicals, including acrylic acid, pyruvic acid, lactide, 1,2-propanediol, and acetaldehyde.[3] The direct catalytic air oxidation of LA is a promising route to pyruvic acid,[4] a key intermediate in the pharmaceutical, agrochemical and food additives sectors.[5] Pyruvic acid occurs naturally as an intermediate product in carbohydrate and protein metabolisms in the body. Since it can be converted to carbohydrates, to fatty acids or energy or to the amino acid alanine, it is a key intermediate in several metabolic processes. Pyruvic acid salts and esters (pyruvates) are used as dietary supplements. For example, calcium pyruvate is used as a fat burner in the food industry. Pyruvic acid is used as a starting material for the synthesis of pharmaceuticals, such as L-tryptophan and L-tyrosine and for the synthesis of amino acids such as alanine and phenyl alanine. Pyruvic acid derivatives are also used to produce crop protection agents, cosmetic agents and flavouring ingredients. It is also a reagent for regeneration of carbonyl compounds from semicarbazones, phenylhydrazones and oximes. Currently, pyruvates are still made via the energy-intensive pyrolysis of tartaric acid with stoichiometric $KHSO_4$ as a dehydrating agent. Ideally, this would be replaced by direct oxidative dehydrogenation using molecular oxygen, giving water as the only by-product. But even though this reaction is thermodynamically feasible, its selectivity is low, because LA is easily over-oxidised.[6]

Several groups have studied this oxidation in vapour and liquid phase. In vapour-phase reactions, various catalysts including iron phosphates and multicomponent mixed oxides were reported.[7-9] But such high-temperature routes are energy intensive, and can lead to the decomposition of pyruvates via decarbonylation or decarboxylation.[10] The side reactions can be suppressed in liquid-phase systems,[11] but the milder conditions typically require noble metal catalysts for oxygen activation.[12] Hayashi *et al.* reported Pd-metal alloy catalysts on activated carbon for the synthesis of pyruvate in the presence of NaOH.[13] Ding and co-workers used Pb-Pt bimetallic supported on carbon materials for the synthesis of pyruvic acid in good yields, using an excess of LiOH to adjust the pH value.[14] Despite these achievements, it's still essential to develop a simple and cost-effective catalytic system for the oxidation of lactates to pyruvates with oxygen under mild conditions.

Vanadium is an abundant element that is often used as a catalyst in the selective oxidation of light alkanes and alcohols.[15] Yasukawa *et al.* studied the oxidation of ethyl lactate to pyruvate over various homogeneous vanadium compounds in a gas-liquid microflow system.[16] They found that vanadium oxytrichloride ($VOCl_3$) gave the highest yield (31%) at room temperature, making it five times as active as V_2O_5.[17] Considering catalyst recovery and product purification, solid vanadium catalysts are preferable.[18] Moreover, the stability of unsupported vanadium compounds is an issue as they are easily hydrolyzed in the presence of H_2O produced during the reaction. Previously, we showed that titania is a suitable support for catalysing the lactate-to-pyruvate reaction.[19] In principle, highly dispersed vanadyl species on anatase TiO_2 are desired for an efficient oxidation. However, the density of isolated vanadyl species is limited by the titania surface area, and distributing the sites evenly on the surface is problematic at high loadings. Besides, these catalysts are also prone to leaching.[20] Based on our earlier experience

with doped mixed oxides for the oxidative dehydrogenation of propane,[21] we hypothesised that doping vanadium ions into the mesoporous TiO_2 lattice would solve these problems. Titania-vanadia hybrids have been made using various methods, including hydrothermal,[22,23] sol-gel,[24] electrochemical,[25] spray pyrolysis[26] and co-precipitation.[27] Gopinath *et al.* studied wormhole-like mesoporous vanadium-doped titania in the oxidative dehydrogenation of ethylbenzene to styrene, attributing the high activity to vanadium atoms in the titania lattice.[28] Yet in most of the cases, the vanadium sites embedded in the titania matrix were unavailable for catalysis. Moreover, mesoporous TiO_2 typically has a low crystallinity, especially when using soft template methods, leading to low stability.[29,30] Thus, we had to find some way to expose the active sites and shorten mass/energy diffusion pathways as well as improve the stability of the catalyst.

Here we report a one-pot synthesis of mesoporous vanadia-titania nanocrystals (meso-VTN) via co-assembly of vanadium and titanium precursors in the presence of an amphiphilic triblock copolymer as templating agent. These new materials feature a large surface area and a high density of isolated vanadium species. These meso-VTN catalysts outperformed the homogenous vanadium complexes and classical VO_x-TiO_2. We also studied the role of various vanadium precursors in the formation of meso-VTN. Only NH_4VO_3, which has the VO_3^- anion, provided a strong electrostatic interaction with the Ti^{4+} cations, yielding an anatase-dominant structure. Increasing the vanadium loading also increases the number of active vanadium dopant sites in the titania lattice, which in turn improves activity and selectivity. We also ran *in situ*-DRIFT spectroscopy studies and DFT calculations, which revealed the relation between the structure of meso-VTN catalyst and its activity in the ethyl lactate oxidation.

RESULTS AND DISCUSSION

Catalyst synthesis and testing. First, co-precursors ammonium metavanadate (NH_4VO_3) and titanium isopropoxide were dissolved in acidic ethanol solution, then, the resultant mixture was assembled with F127 template via evaporation-induced self-assembly. Subsequent calcination removed the template (Figure S1), yielding a highly crystalline meso-VTN (denoted as NH_4VO_3@VTN). Three other meso-VTN materials were prepared similarly, starting from different vanadium precursors ($VOSO_4$, $VO(acac)_2$ and VCl_3, see the experimental section for details).

We then studied the catalytic performance of these meso-VTN materials in the liquid-phase aerobic oxidation of ethyl lactate to ethyl pyruvate (Table 1). Compared to homogeneous vanadium complexes, all the meso-VTN samples showed good catalytic activity and higher turnover frequencies (TOFs). Control reactions showed that the vanadium precursors themselves were active as oxidation catalysts, but not selective. Besides the intrinsic disadvantages of homogeneous catalysts in catalyst recovery and product purification, the homogeneous vanadium compounds are unstable, and are easily hydrolyzed by the water by-product.[31,32] In contrast, our meso-VTN solid can be reused at least ten times without losing activity (see recycling experiments below). The highest TOF of 118 h^{-1} was measured for NH_4VO_3@VTN.

Table 1. Oxidative dehydrogenation of ethyl lactate with O_2 to ethyl pyruvate over various catalysts [a]

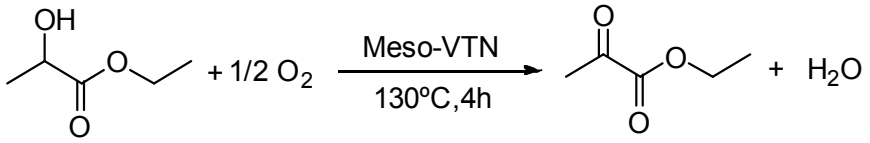

Ethyl lactate — Ethyl pyruvate

Entry	Catalyst	Conversion (%) [b]	Selectivity (%)	Yield (%) [b]	TOF [c] (h^{-1})
1	VCl_3	63.9	12.3	7.9	0.5
2	$VOSO_4$	63.4	32.9	20.9	1.4

3	$VO(acac)_2$	79.9	64.1	51.2	5.7
4	NH_4VO_3	64.3	72.6	46.7	2.3
5	V_2O_5	13.9	61.8	8.6	0.3
7 [d]	VCl_3@VTN	20.8	85.1	17.7	61
8 [e]	$VOSO_4$@VTN	25.6	71.3	18.3	86
9 [f]	$VO(acac)_2$@VTN	28.8	78.5	22.6	97
10 [g]	NH_4VO_3@VTN	34.6	89.4	30.9	118

[a] Reaction conditions: amount of all catalysts 50 mg, Temperature: 130 °C. 1 atm O_2, 4h. Ethyl lactate 8.5mmol (1.0 g); diethyl succinate (solvent, 2 ml). [b] Determined by GC using biphenyl as an internal standard. [c] Turnover frequency for ethyl pyruvate formation calculated as moles of ethyl pyruvate per moles of total vanadium per hour). [d] VCl_3@VTN (0.6 wt.% V, determined by ICP analysis); [e] $VOSO_4$@VTN (0.5 wt.% V); [f] $VO(acac)_2$@VTN (0.5 wt.% V); [g] NH_4VO_3@VTN (0.6 wt.% V).

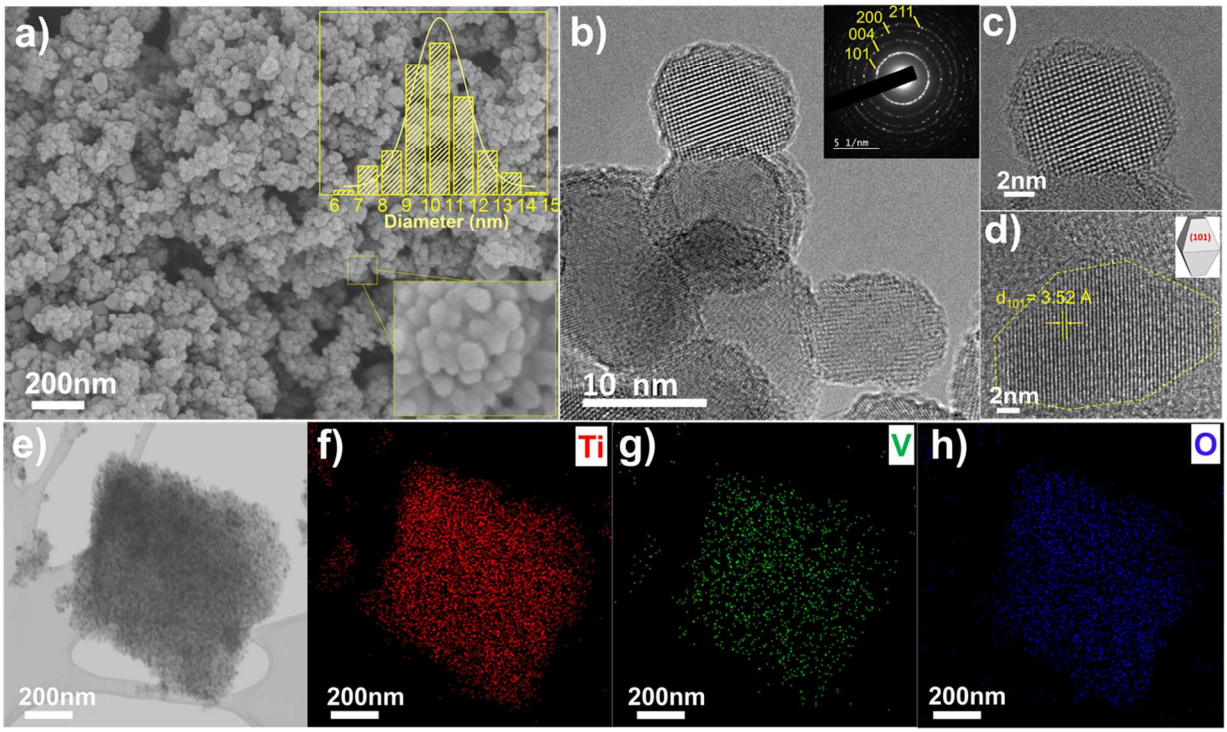

Figure 1. (a) SEM image of NH_4VO_3@VTN, inset: particle size distribution (top right) and enlarged SEM image of NH_4VO_3@VTN nanospheres (bottom right); (b) Representative TEM image of NH_4VO_3@VTN and the corresponding SAED pattern (inset); (c) magnified HRTEM image of NH_4VO_3@VTN; (d) crystal plane indexing of NH_4VO_3@VTN, the inset shows the

crystallite shape; (e) STEM image and (f, g, h) corresponding elemental mappings of Ti, V and O in an NH_4VO_3@VTN sample.

To understand the high performance of NH_4VO_3@VTN, we characterized the catalysts. The scanning electron microscopy (SEM) images of the NH_4VO_3@VTN samples show highly uniform and nearly spherical morphology in large domains (Figure 1a). The VTN nanoparticles have a rough surface with an average size of ~10 nm (see inset in Figure 1a). This size agrees well with the size obtained from the high-resolution transmission electron microscopy (HRTEM) studies (Figure 1b and 1c). HRTEM also confirmed the VTN uniformity. A large number of white dots can be observed by the TEM over the entire nanostructure, indicating that the mesoporosity is well-dispersed in the VTN framework (see supporting information, Figure S2).[33,34] The corresponding selected-area electron diffraction (SAED) pattern confirmed a set of diffraction rings (inset in Figure 1b), in accordance with the crystalline anatase phase (JCPDS, no. 21-1272). Figure 1d also shows the clear lattice fringes with an interplanar distance of 3.52 Å, matching well with the (101) planes of the anatase structure.[35] In addition, the high-angle annular dark-field scanning TEM (HAADF-STEM) images and corresponding elemental mapping further demonstrated the uniform distribution of Ti, V and O atoms in the NH_4VO_3@VTN sample (Figure 1e-1h and Figure S3).[36,37]

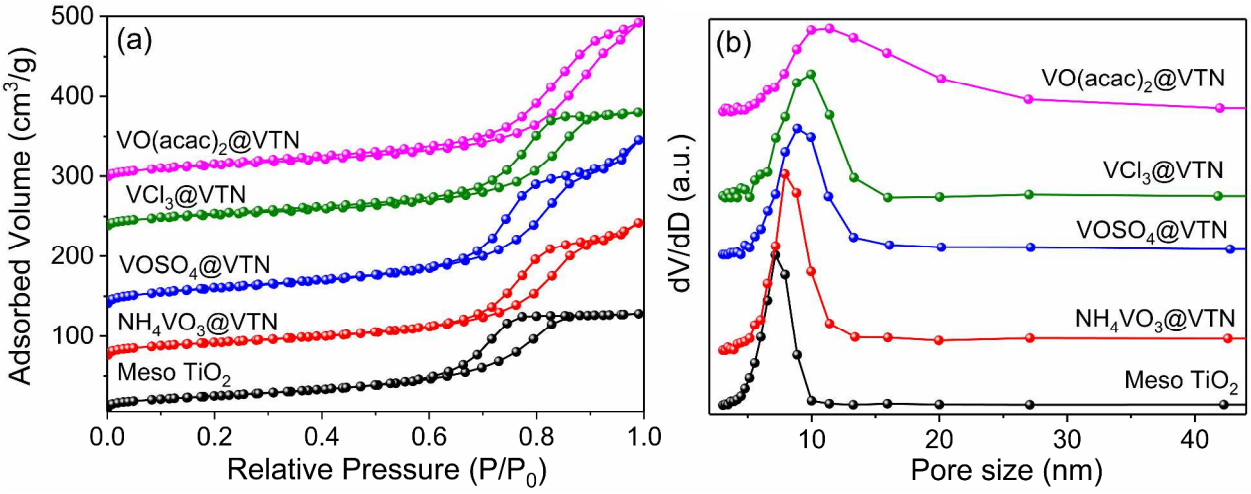

Figure 2. The Nitrogen adsorption-desorption isotherms (a) and BJH pore size distribution curves (b) of pure TiO_2 and meso-VTN materials prepared from different V precursors.

Then nitrogen adsorption-desorption experiments for the various meso-VTN samples were performed (Figure 2a). All the materials showed a typical type IV isotherm with a H1-type hysteresis loop, suggesting the presence of mesopores.[38] Table 2 summarizes the textural parameters. The BET area and pore volume of NH_4VO_3@VTN were as high as 112 m^2g^{-1} and 0.33 cm^3g^{-1}, comparable with pristine TiO_2. When using other vanadium precursors, the capillary condensation step becomes less steep and shifts to high relative pressure, indicating a gradual increase in pore size.[39] This trend agrees well with the results of pore size distribution (Figure 2b), where NH_4VO_3@VTN showed a sharp peak indicating uniform pore size, while the peaks of $VOSO_4$@VTN, VCl_3@VTN and $VO(acac)_2$@VTN became broad. This difference indicates the key role of vanadium precursors in the formation of meso-VTN. The increase in pore size can be attributed to the different strengths of electrostatic interaction between Ti and V precursors during the self-assembly process. [40,41]

Table 2. The textural parameters of meso-VTN materials.

Sample	Vanadium	Anatase: rutile [b]	S_{BET}	Pore volume,	Pore diameter,

	loading (wt.%) [a]		(m^2g^{-1}) [c]	$V_P\,(cm^3g^{-1})$ [c]	D_p (nm) [d]
mesoporous TiO_2	–	>100:1	121	0.2	7.1
NH_4VO_3@VTN	0.59	95:5	112	0.33	7.9
$VOSO_4$@VTN	0.46	90:10	93	0.27	8.9
$VO(acac)_2$@VTN	0.5	81:19	87	0.31	10
VCl_3@VTN	0.6	41:59	82	0.23	8.8

[a] Determined by ICP analysis. [b] The weight percentage of the rutile phase was calculated using the formula: $W_R=1/\ [1+0.884(A_A/A_R]$, where A_A and A_R represent the XRD integrated intensities of anatase (101) and rutile (110) diffraction peaks. [c] Calculated based on N_2 sorption at 77 K. [d] Calculated from BJH method.

X-ray diffraction (XRD) can verify the influence of V doping on the crystalline structure of meso-VTN. As shown in Figure 3a, no vanadia peaks were detected, suggesting a uniform distribution of vanadium in the VTN crystals, in agreement with the elemental mapping shown in Figure 1. Notably, the (101) diffraction peak shifts slightly towards a higher angle after the introduction of vanadium species (Figure 3b). This implies that the vanadium ions are incorporated in the titania lattice.[42] For NH_4VO_3@VTN, the XRD pattern showed the characteristic anatase titania peaks, with a trace amount of rutile. However, with other vanadium compounds as precursors,

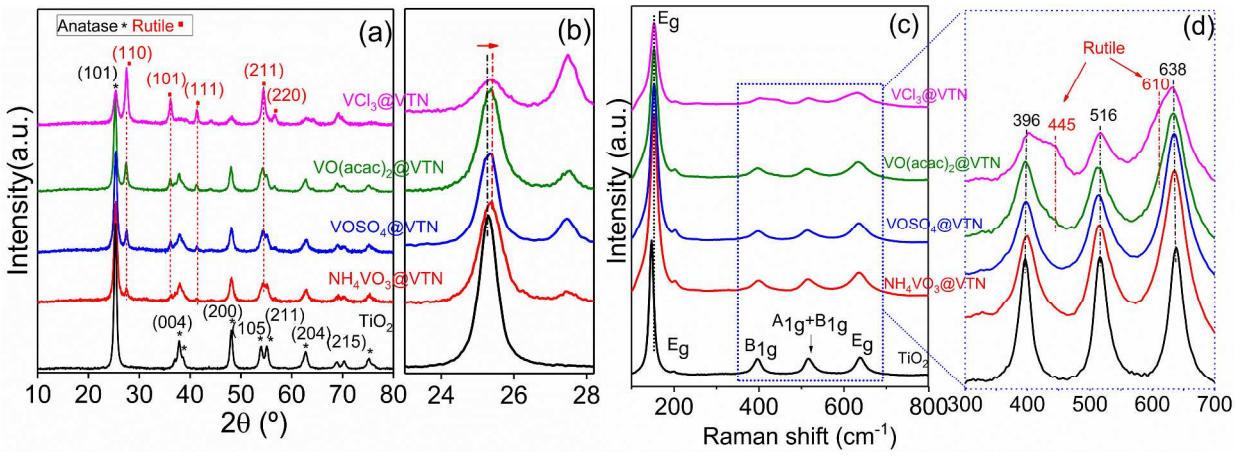

Figure 3. X-ray diffraction patterns (a, b) and Raman spectra (c, d) of blank-TiO_2 and VTN materials prepared from different vanadium precursors. Due to the low loadings, VO_x species were not observed.

the intensity of the rutile diffraction peaks increased while the anatase fraction decreased. Notably, VCl_3@VTN showed a rutile-dominant diffraction pattern. The anatase : rutile ratios, calculated based on the integrated intensities of anatase (101) peak and rutile (110) peak,[43] are shown in Table 2. The anatase content in meso-VTN decreases as follows: NH_4VO_3 > $VOSO_4$ > $VO(acac)_2$ > VCl_3. This confirms that the vanadium-induced phase transition of meso-VTN from anatase to rutile depends strongly on the vanadium precursor. Figure 3c shows the Raman spectra of all V doped VTN samples. The Raman characterization also upholds the XRD results. All the samples showed a set of bands at 146 (E_g), 198 (E_g), 396 (B_{1g}), 516 (A_{1g}+B_{1g}) and 638 (E_g) cm^{-1}, which are assigned to the fundamental active modes of anatase TiO_2.[28,44] No typical Raman peaks of VO_x species were detected, indicating the absence of crystalline vanadium oxides, also supporting the complete doping of vanadium into the anatase lattice.[45] Besides, all the peaks of VTN samples became asymmetric compared to pure TiO_2 (Figure 3d). This holds

especially for $VO(acac)_2$ and VCl_3@VTN, where two weak bands at 445 cm^{-1} and 610 cm^{-1} were observed, which can be assigned to the rutile TiO_2 features.[43] Among those vanadium precursors, only NH_4VO_3 has the VO_3^- anion, which could provide a strong electrostatic interaction with the Ti^{4+} cations, showing a more anatase-dominant structure. Note that both anatase and rutile titania are made up of TiO_6 octahedra in tetragonal configurations.[46] The structural difference between them is caused by the stacking arrangement of these TiO_6 units. The metastable anatase structure consists of edge-sharing TiO_6 octahedra in zig-zag stacking, while the stable rutile consists of both corner and edge-sharing TiO_6 in the linear stacking.[47,48] Titanium oligomers can interact with vanadium precursors via electrostatic interaction during the self-assembly process.[49] The substitution of the lattice Ti by V ions distorts the anatase structure, thus promoting the transformation from anatase to rutile.

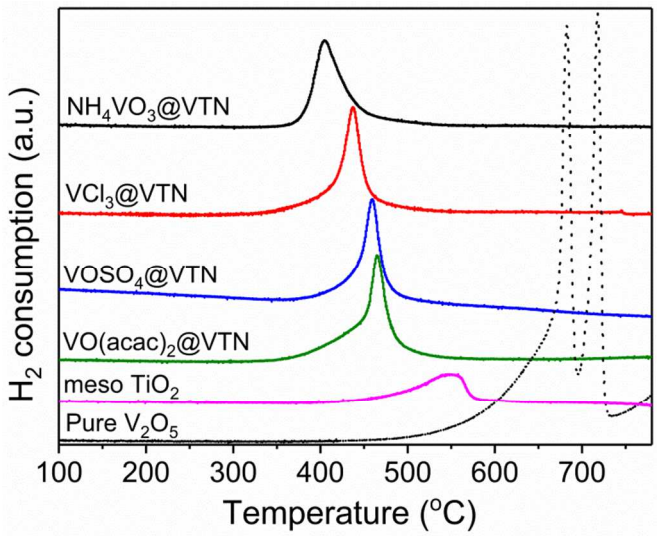

Figure 4. H_2-TPR profiles of TiO_2, V_2O_5 and VTN materials with different V precursors.

Temperature-programmed reduction studies showed that NH_4VO_3 forms monomeric VO_4 units. (Figure 4). After introducing vanadium into the titania lattice, the maximum hydrogen

consumption (T_{max}) shifted to lower temperature, compared with pure TiO_2 and V_2O_5. Generally, the nature of the VO_x species affects the reducibility of V-doped TiO_2. Monomeric VO_4 species are more easily reduced.[50] Among the VTN samples, NH_4VO_3@VTN showed the lowest T_{max}, suggesting that NH_4VO_3@VTN forms more monomeric vanadium species. This may reflect the strong electrostatic interaction between VO_3^- with the Ti^{4+} precursors. We conclude that NH_4VO_3 is the best precursor, as it provides a strong electrostatic interaction with the Ti^{4+} cations, thereby suppressing the agglomeration of vanadium species (Scheme 1).

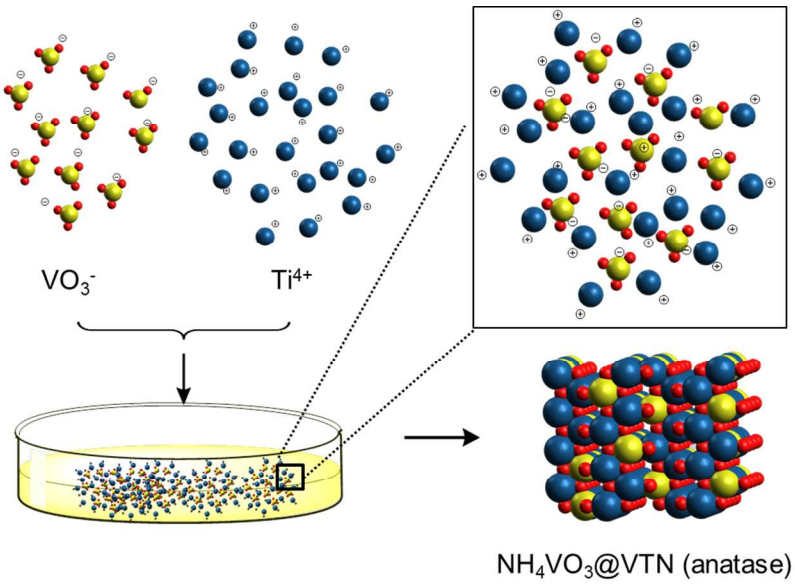

Scheme 1. Schematic illustration of the synthesis route of NH_4VO_3@VTN via electrostatic interaction between the VO_3^- and the Ti^{4+} precursors.

Factors governing activity and selectivity.

We examined the effect of reaction conditions on the aerobic oxidation of ethyl lactate with dioxygen over the NH_4VO_3@VTN catalyst. As shown in Figure 5, the selectivity of ethyl pyruvate was high at lower temperatures and decreased gradually with increasing temperature.

Ethyl lactate conversion increased with the reaction temperature, with the highest yield to ethyl pyruvate obtained at 130 °C. Increasing the temperature further decreased the yield of ethyl pyruvate. We also plotted the selectivity of major products against ethyl lactate conversion and reaction time over 0.6%V-NH_4VO_3@VTN at optimized temperature. As shown in Figure 6a, the ethyl lactate conversion increased with the reaction time reaching 70% after 8 h, with ethyl pyruvate as the main product together with ethanol, pyruvic acid and some minor by-products. The ethyl pyruvate selectivity gradually decreased from 91% to 58% with the reaction time on stream, as the amounts of both ethanol and pyruvic acid increased to 28% and 11%, respectively. Several minor by-products including acetic acid and acetaldehyde were detected at a steady state with a selectivity of ~2 %. Based on these results, we propose a reaction network for the aerobic oxidation of ethyl lactate, involving oxidative dehydrogenation, hydrolysis and decarboxylation steps (Figure 6b).

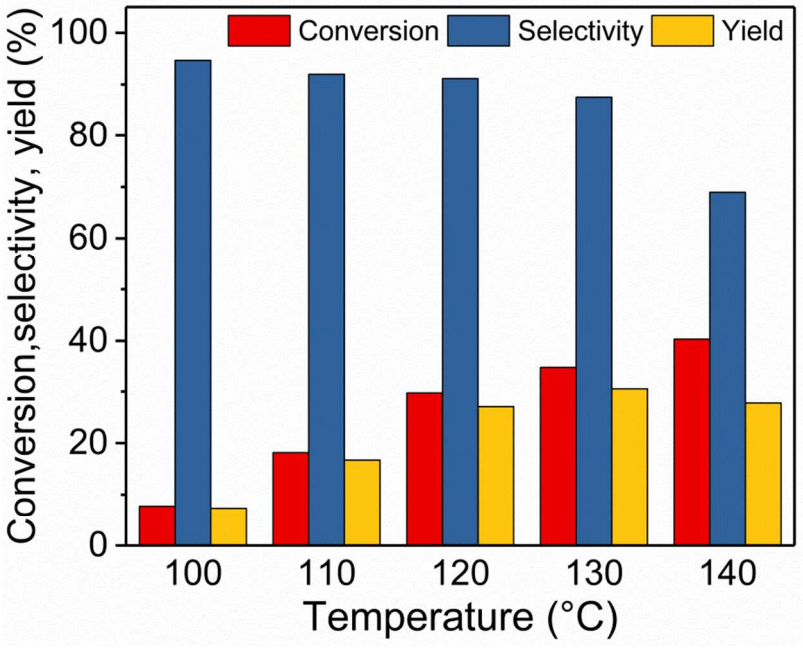

Figure 5. Effect of reaction temperature on the aerobic oxidation of ethyl lactate. Reaction conditions: 0.6%V-NH_4VO_3@VTN 50mg, 1 atm O_2, 2 h. ethyl lactate 8.5 mmol (1.0 g), diethyl succinate (solvent, 2 ml).

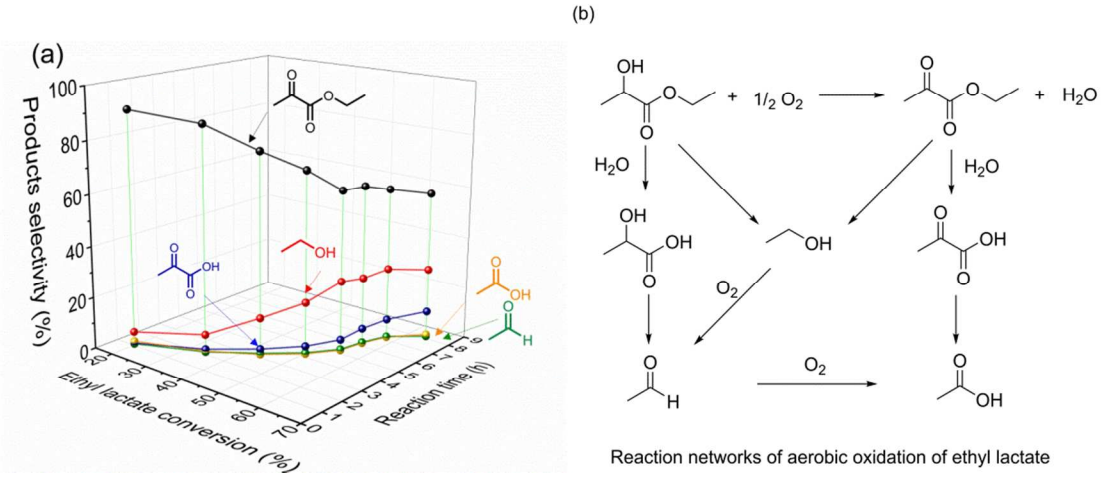

Figure 6. (a) Plots of product selectivity against ethyl lactate conversion and reaction time; Reaction conditions: 0.6%V-NH_4VO_3@VTN 50mg, 1atm O_2, temperature: 130 °C. Ethyl lactate 8.5 mmol (1.0 g), diethyl succinate (solvent, 2 ml). (b) Proposed reaction pathway for the aerobic oxidation of ethyl lactate.

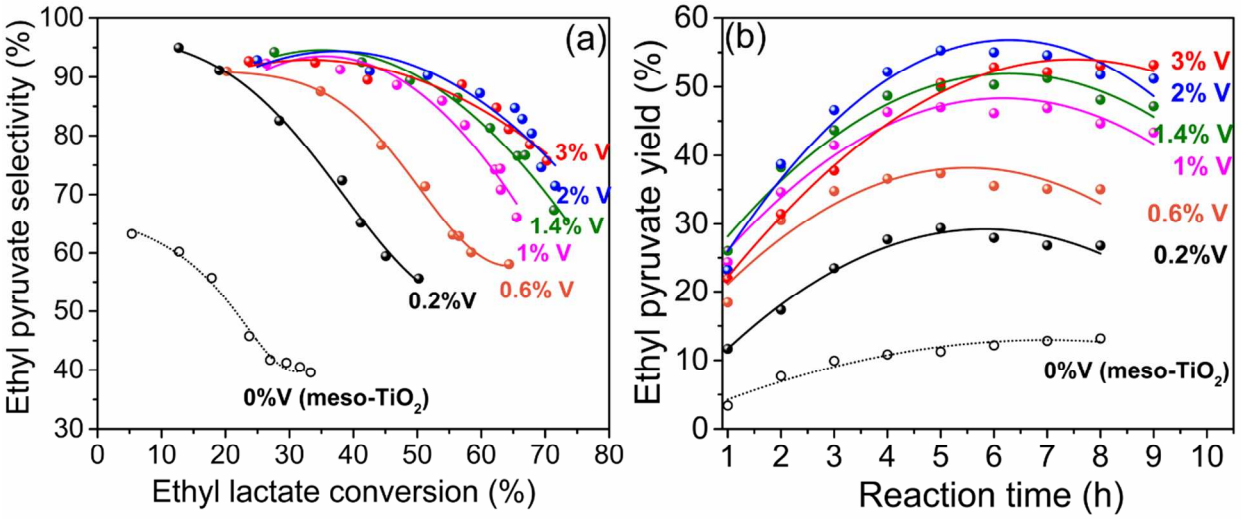

Figure 7. Selectivity to ethyl pyruvate plotted against conversion (a) of NH_4VO_3@VTN varying the vanadium loading from 0 to 3 wt.%, and (b) the corresponding time-resolved yield profile of ethyl pyruvate; Reaction conditions: catalyst 50 mg, 1 atm O_2, 130 °C, ethyl lactate 8.5 mmol (1.0 g), diethyl succinate (solvent, 2 ml).

We also studied the effect of vanadium loading on the catalytic activity by modifying the NH_4VO_3 precursor concentration for a series of NH_4VO_3@VTN materials. These catalysts are denoted as *x*V-NH_4VO_3@VTN, where *x* represents the weight ratio (wt. %) of vanadium. The corresponding porosity analysis and textural parameters are given in supporting information (Figure S4 and Table S1). Figure 7a shows the selectivity-conversion curves of these NH_4VO_3@VTN catalysts. Pure meso-TiO_2 (0% V) showed some conversion, but selectivity to pyruvate was low. We think that the basic OH groups on TiO_2 surface can hydrolyse lactate and pyruvate to ethanol and lactic/pyruvic acid. When vanadium was introduced in TiO_2, the resulting VTN catalysts showed high ethyl pyruvate selectivity reaching 95% at low ethyl lactate conversion. At higher ethyl lactate conversions, the selectivity of ethyl pyruvate tended to increase with an increase in the V loading (from 0.2% to 2%V).[9] This indicates that vanadium acts as the active site in lactate-to-pyruvate reaction, and at higher vanadium loadings, the competing hydrolysis is suppressed. To check this, we ran the control experiments on the aerobic oxidation of ethyl lactate over a 0.2V%-NH_4VO_3@VTN, using molecular sieve-3Å (MS-3A) as a dehydrating agent (Figure S5). Addition of MS-3A gave a much higher selectivity of 80% to ethyl pyruvate (at 51.6 % conversion), compared to 56 % (at 50.2 % conversion) in the absence of MS-3A (Figure S5a). Without the dehydrating agent, the amount of by-products was higher; e.g. selectivity of ethanol 22 % instead of 10% (Figure S5b). Upon increasing V loading to 3%, the difference between 2% and 3% almost leveled-up. To understand better this trend, we plotted the ethyl pyruvate yield against reaction time (Figure 7b), which confirms that 2%V-NH_4VO_3@VTN gives highest yield. Indeed, the crystalline V_2O_5 can be seen in the XRD of the 3%V NH_4VO_3@VTN sample, suggesting that some of the vanadium is aggregated as V_2O_5 (see Figure S6 in the supporting information). Thus, increasing the vanadium loading also increases

the number of active vanadium dopant sites in the titania lattice, which in turn results in improved overall activity and selectivity.

Further insight into the reaction can be gained by analysing structure-activity relationships. Interestingly, we found that the TOF of NH_4VO_3@VTN was inversely proportional to the vanadium loading (Figure 8a), showing a close correlation with the ratio of $V^{4+}/ (V^{4+}+V^{5+})$ (derived from V2*p* spectrum in Table 3). In particular, the amount of exposed V^{4+} ions are correlated with catalytic performance. The similar ionic radii of Ti^{4+} (0.61 Å) and V^{4+} (0.58 Å) enable the doping of the latter into the titania lattice (V^{5+} is much smaller, 0.54 Å).[45] To understand this behaviour at the atomic level, we built a simple model of anatase titania (Figure 8b), and performed the density functional theory (DFT) calculations of the substitution of V^{4+} and V^{5+} for Ti^{4+} in anatase lattice (A more detailed description of the simulations is provided in the supporting information). We found that exchanging the surface Ti with V^{4+} on anatase TiO_2 corresponds to a lower energy than that of V^{5+}, in line with previous reports.[51]

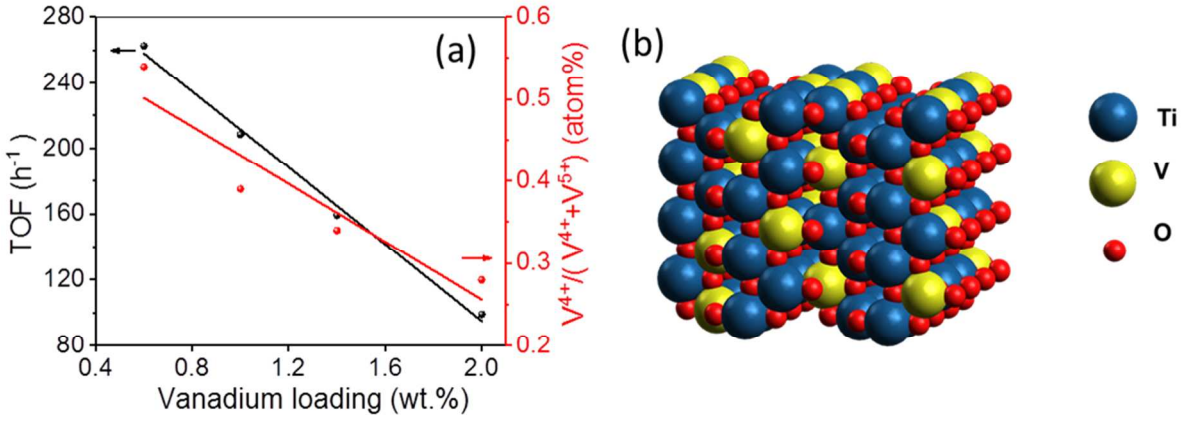

Figure 8. (a) Relationship between turnover frequency (TOF) for ethyl pyruvate formation, $V^{4+}/(V^{4+}+V^{5+})$ (at. %) and vanadium loading catalysts. Reaction conditions: NH_4VO_3@VTN 50mg, 1 atm O_2, 1h, ethyl lactate 8.5 mmol (1.0 g), Solvent: Diethyl succinate 2ml. (b) A model of NH_4VO_3@VTN, Atom colors: Ti, blue; O, red; V, yellow.

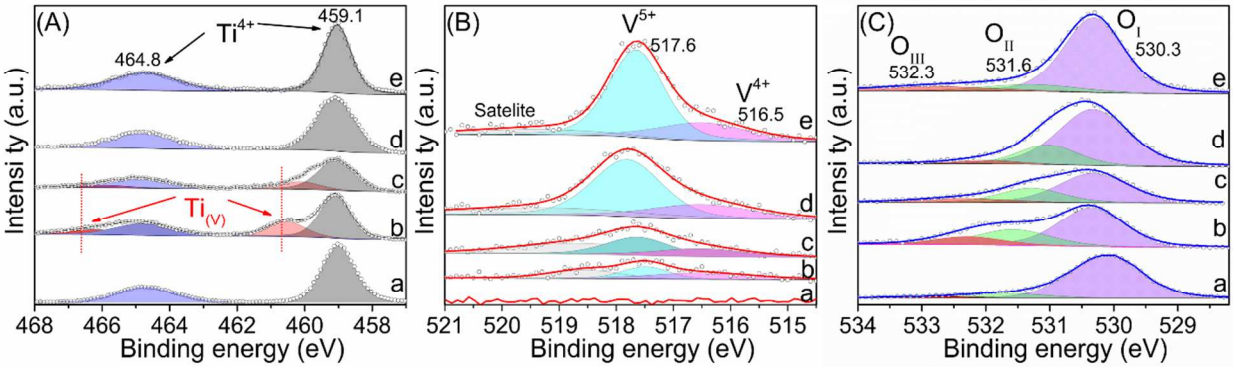

Figure 9. XPS studies showing high resolution Ti 2p spectra (A), high resolution V2p spectra (B) and high resolution O1s spectra (C) of the NH_4VO_3@VTN with different V loadings: (a) 0%V (meso-TiO_2), (b) 0.6%V, (c) 1%V, (d) 1.4%V and (e) 2%V.

X-ray photoelectron spectroscopy (XPS) measurements show that the Ti 2*p* peaks of NH_4VO_3@VTN containing 0.6% V and 1% V are asymmetric, compared with pure TiO_2 (Figure 9A, a, b and c). This indicates the presence of two types of Ti on the surface. The binding energy corresponding to Ti^{4+} (Ti $2p_{1/2}$: 464.8 eV and Ti 2 $p_{3/2}$: 459.1 eV) is shifted towards higher values. These results imply that Ti is replaced with V, decreasing electron charge density of the Ti^{4+}.[52] This means that the neighboring lattice Ti (denoted as $Ti_{(V)}$) of the vanadium dopant gives a high binding energy. For comparison, we prepared 0.6% VO_x/TiO_2 using impregnation, where the $Ti_{(V)}$ peak was not detected in XPS spectra (Figure S7). This further confirmed the substitution of lattice Ti by vanadium. As the vanadium loading increases, the deconvoluted peaks corresponding to $Ti_{(V)}$ gradually disappear (Figure 9A, d and e). When more vanadium is incorporated in TiO_2 lattice, isolated V^{4+} will be gradually converted to polymerized VO_x, thus lowering the fraction of $Ti_{(V)}$.[53] This agrees also with the decrease of $\frac{V^{4+}}{V^{4+}+V^{5+}}$ ratio (Figure 9B and Table 3). When the V loading is increased to 3%, the peaks of crystalline V_2O_5 can be seen in the XRD pattern (Figure S6). As shown in Figure 9C, the spectra of the O*1s* in

NH_4VO_3@VTN can be deconvoluted into three peaks: the peak at 530.3 eV was ascribed to the O^{2-} lattice oxygen (O_I); and the peaks at ~531.6 eV and ~532.3 eV are ascribed to O_2^{2-} and O^- surface chemisorbed oxygen (labelled as O_{II} and O_{III}).[54] The O_{II} oxygens, which are located at the surface defects, are more active and therefore more easily reduced.[55,56] As vanadium ions with different valences replace Ti^{4+} ions in the lattice, the charge imbalance generates structural defects and additional oxygen vacancies.[57,58] This increases the number of mobile O_{II} species.[59] In our case, the $V^{4+}/(V^{4+}+V^{5+})$ ratio decreased from 0.54 to 0.28 when V loading is increased, and the $\frac{O_{II}}{O_I+O_{II}+O_{III}}$ fraction decreased simultaneously.

Table 3. Surface atom ratios of NH_4VO_3@VTN calculated from XPS analysis.

Sample	V^{5+} (at %)	V^{4+} (at %)	O_I (at %)	O_{II} (at %)	O_{III} (at %)	$V^{4+}/(V^{4+}+V^{5+})$	$O_{II}/(O_I+O_{II}+O_{III})$
Meso-TiO_2	-	-	52.7	6	2.2	-	0.10
0.6%V-NH_4VO_3@VTN	1.13	1.32	38.05	17.1	6.83	0.54	0.28
1%V-NH_4VO_3@VTN	1.77	1.12	33.43	15.14	7.51	0.39	0.27
1.4%V-NH_4VO_3@VTN	2.52	1.35	39.52	14.37	4.08	0.34	0.25
2%V-NH_4VO_3@VTN	4.07	1.57	45.38	13.32	2.48	0.28	0.22

Leaching of active species into the solution is a known problem in heterogeneous catalysis. To rule out the possibility of vanadium leaching, we ran a hot filtration experiment (Figure S8).[60] When the NH_4VO_3@VTN catalyst was filtered from the reaction mixture after 3 h, no further ethyl lactate conversion was observed. Moreover, the vanadium content of the filtrate was below the detection limit of ICP-AES analysis. For comparison, we prepared vanadia supported on titania with an identical surface vanadium content using impregnation (herein VO_x/TiO_2; the vanadium content on the surface was determined by XPS). Mesoporous anatase TiO_2 was impregnated with aqueous solutions of NH_4VO_3 and oxalic acid, followed by drying and calcining for 4 h at 500 °C. Control experiments showed that the filtrate of VO_x/TiO_2 was still active in ethyl lactate oxidation (Figure S9), indicating that V species do leach into solution in the case of impregnation. We also run the recyclability of NH_4VO_3@VTN. In each run, the catalyst was separated by simple centrifugation, then dispersed in water under ultra-sonication for 1 h. As shown in Figure 10, the NH_4VO_3@VTN could be reused ten times without significant loss of activity. The XRD and TEM analysis confirmed that the meso-structure and anatase/rutile ratio were well preserved after recycling (Figure S10).

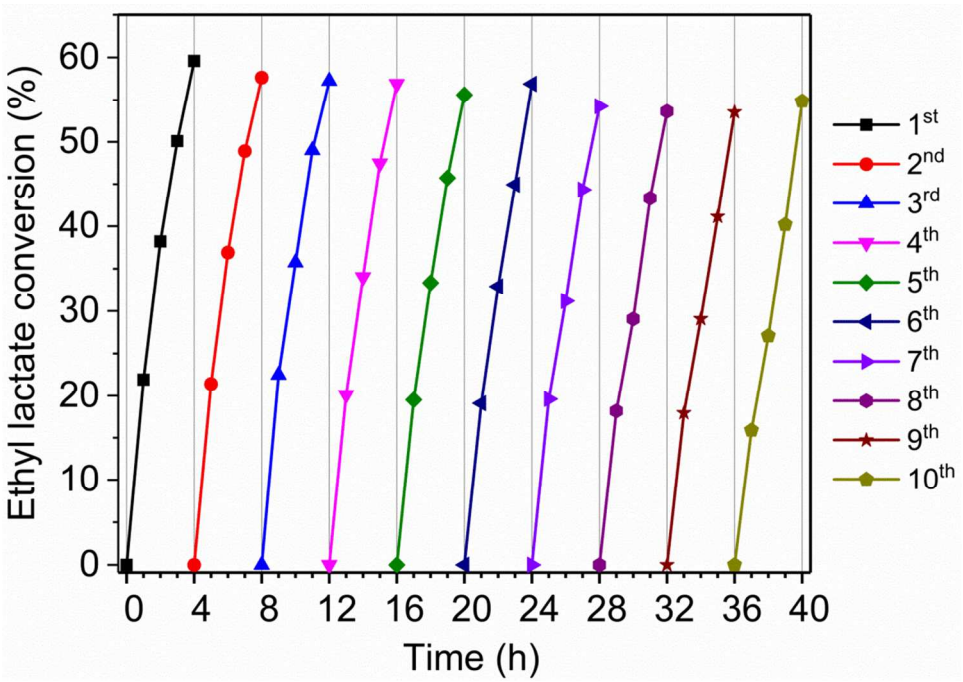

Figure 10. Kinetic plots of recycling tests of NH_3VO_4@VTN in the oxidation of ethyl lactate to ethyl pyruvate. Reaction conditions: 100 mg catalyst, 130 °C, 1 atm O_2, 4 h. Ethyl lactate 8.5 mmol (1 g), diethyl succinate (solvent, 2 ml).

Mechanistic considerations.

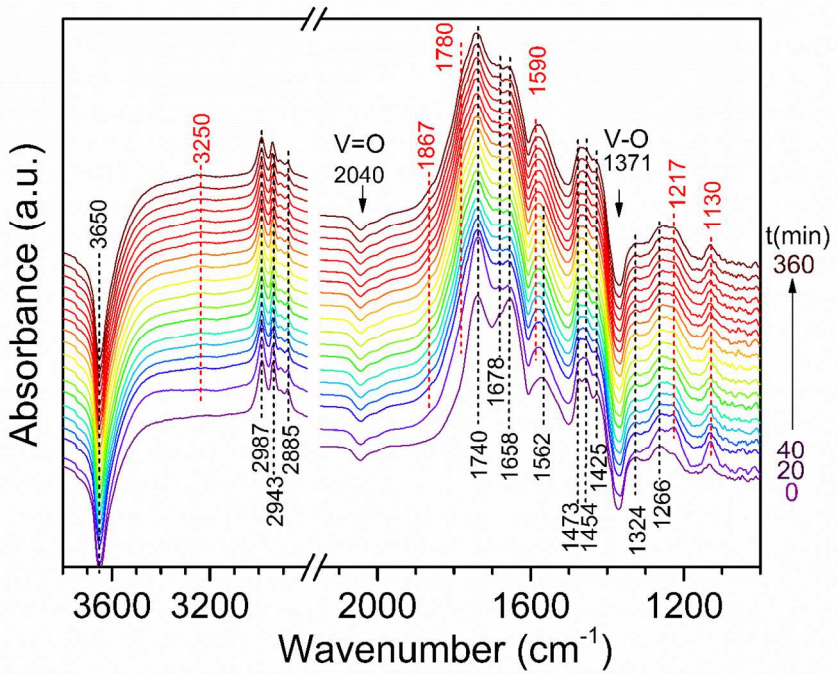

Figure 11. In situ DRIFT spectra recorded during aerobic oxidation of ethyl lactate with air over 0.2%-NH_3VO_4@VTN catalyst at different time intervals (0, 20, 40, ⋯, 360 min) at 130 °C.

To study the reaction mechanism of lactate-to-pyruvate on the NH_3VO_4@VTN surface, we did *in situ* DRIFTS studies. Figure 11 shows the results for the aerobic oxidation of ethyl lactate over 0.2%V-NH_3VO_4@VTN at 130 °C at different reaction times. Typical vibrational bands of ethyl lactate on NH_3VO_4@VTN were observed after ethyl lactate adsorption. The positive bands at 2987 cm^{-1}, 2943 cm^{-1}, 2885 cm^{-1} were ascribed to $\nu_{as}(CH_3)$, $\nu_{as}(CH_2)$, $\nu_s(CH_3)$, respectively. [61,62] The corresponding C–H bending vibrations were also detected ($\delta(CH_2)$ =1473 cm^{-1}, $\delta(CH_3)$ =1454 cm^{-1} and $\delta(CH_3)$ = 1324 cm^{-1}).[61,63] The lactate carboxyl stretching vibrations were observed at 1562 cm^{-1} (ν_s (COO)) and 1425 cm^{-1} (ν_{as} (COO)), while the peak at 1740 cm^{-1} belongs to the lactate carbonyl ν(C=O).[61] Two additional peaks appeared at 1678 cm^{-1} and 1658 cm^{-1}, probably due to the C=O bonds coordinated with VTN surface.[64] After 20 min, we observed two new shoulder peaks at 1867 cm^{-1} and 1780 cm^{-1}, which are related to the carbonyl

stretching of the α-keto group of the pyruvate.[65] The intensity of pyruvate bands increased with the reaction time on stream; meanwhile, the ν_s(COO) at 1562 cm^{-1} gradually shifted to 1590 cm^{-1}, suggesting the formation of more ethyl pyruvate. Moreover, two weak bands at 1130 cm^{-1} and 1217 cm^{-1} can be ascribed to the hydroxyl-related C–O vibrations of ethyl lactate [$\nu_{lactate}$(C–O) and $\delta_{lactate}$(C–O)], reflecting the OH deprotonation of ethyl lactate on VTN surface. The signals of $\nu_{lactate}$(C–O) and $\delta_{lactate}$(C–O) reached the maximum at first 20min, indicating that the lactate OH deprotonation plays a key role in this reaction. This is also confirmed by the new broad band at ~3250 cm^{-1} , which indicates the formation of adsorbed water on VTN surface.[65] Note that the V=O overtone band (~2040 cm^{-1}) [63] is well preserved during the aerobic oxidation of ethyl lactate, while the V–O related bond [δ (V^{4+}–O–Ti) ~1370 cm^{-1}][66] is diminished in intensity. This indicates that the terminal V=O bonds are not involved in the ethyl lactate conversion, confirming the vital role of V^{4+}–O related bonds.

To complement the experimental results and the reaction pathways for the oxidative dehydrogenation of ethyl lactate to ethyl pyruvate, we built a periodic model of VTN by replacing lattice Ti with V^{4+} in the top layer of the (101) facet of anatase titania. This model was simulated using density functional theory (DFT) calculations as implemented in the CP2K package (see supporting information for details). First, we studied the adsorption and dissociation of ethyl lactate (EL) on the VTN surface. Several possible adsorbed forms were considered (see Figure S11). Geometry optimization showed that EL can be stabilized on either surface titanium or vanadium atoms (Figure 12). The hydroxyl oxygen coordinates to surface titanium atoms with a Ti···OH-R distance of 2.085 Å, compared with a V···OH-R distance of 2.126 Å. In both cases, the O–H bonds were elongated, from 0.974 Å to 1.039 Å and 1.025 Å,

respectively. The adsorption energy of EL on Ti was higher than that of EL on V by 0.73 kcal/mol, in agreement with previous reports.[19]

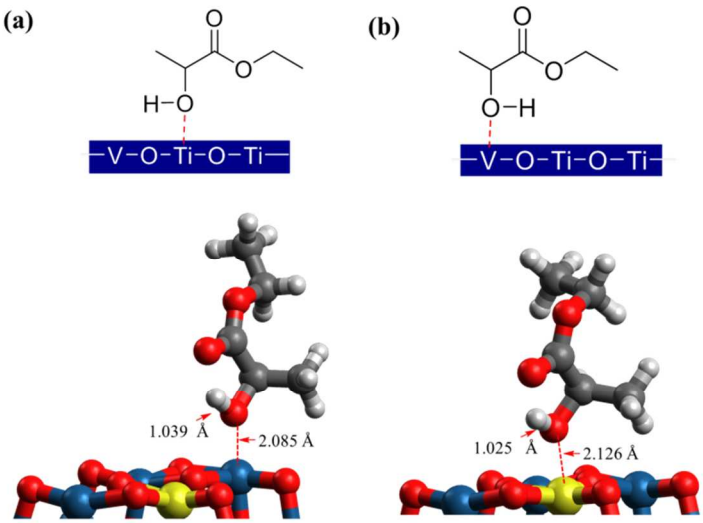

Figure 12. Optimized geometries of two different model for ethyl lactate chemisorption on VTN (101) surface. (a) Ti-type adsorption geometry, where ethyl lactate interacts with Ti atom; (b) V-type adsorption geometry, where ethyl lactate interacts with V atom. Atom colors: Ti, blue; O, red; V, yellow.

Then, the activation of hydroxyl group triggers the dissociation of EL via proton transfer to a nearby bridging oxygen atom (O_{br}). To simplify this process, we focused on two types of bridges: V^{4+}–O–Ti ($O_{br\text{-}V}$) and Ti–O–Ti ($O_{br\text{-}Ti}$). Figure 13 shows the geometries of two possible intermediates, (a) and (b), in this step. In both cases, the the protonated EL is bonded to a titanium atom. Yet while in (a) the hydroxyl H transfers to a nearby V^{4+}–O–Ti site, forming a H-$O_{br\text{-}V}$ bond, in (b) the proton transfers to a Ti–O–Ti to form a H-$O_{br\text{-}Ti}$ bond. The intermediate energy for the formation of (a) and (b) are -75.6 kcal/mol and -136 kcal/mol, respectively. This suggests that the V^{4+}–O–Ti bonds are responsible for the dissociation of ethyl lactate over VTN catalysts, supporting the experimental result. Besides, the β-hydrogen of the protonated EL can interact with the V^{4+}–O–Ti oxygen, increasing the C-H_β bond length from 1.099 Å to 1.118 Å.

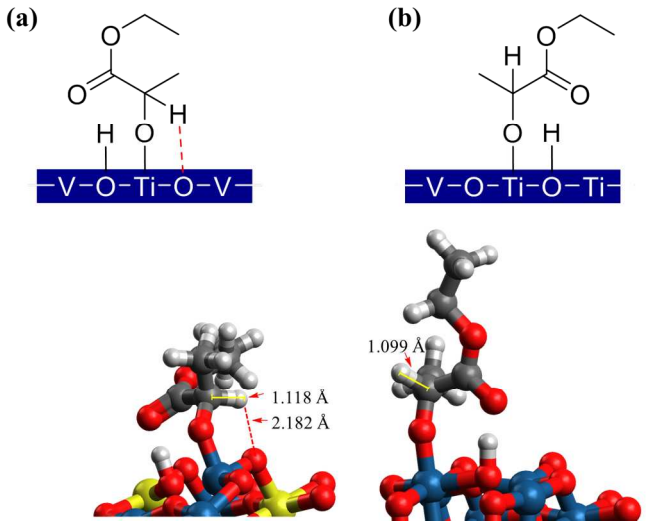

Figure 13. Representative structures of the two intermediates during proton transfer process. (a) Hydrogen atom transfer to bridging oxygen atoms in V–O–Ti sites; (b) Hydrogen atom transfer to bridging oxygen atoms in Ti–O–Ti sites.

Therefore, the simulations show us that: *(i)* ethyl lactate adsorbs preferentially on the VTN surface via the coordination of hydroxyl oxygen to titanium; *(ii)* V^{4+}–O–Ti bonds play a vital role in the dissociation of ethyl lactate; and *(iii)* the deprotonation of β-hydrogen is also activated by V^{4+}–O–Ti bonds.

For most oxidative dehydrogenation reactions, the molecular oxygen activation involves either free-radical or Mars-Van Krevelen pathways.[67] To determine if any radical species is involved in this reaction, we introduced a number of free radical scavengers to the reaction mixture (BHT, *p*-benzoquinone and *tert*-butyl alcohol, see Table S2). These free-radical scavengers did not suppress the reaction completely, ruling out the formation of free-radical intermediates (i.e., superoxide radical $\bullet O_2^-$) in the bulk reaction mixture. To further study the role of molecular oxygen, we ran control experiments over NH_4VO_3@VTN, where the molecular oxygen was replaced by nitrogen. The reaction was limited without oxygen.[55,56] Thus, we can conclude that

the aerobic oxidation follows a Mars-Van Krevelen mechanism for VTN catalysts, wherein molecular oxygen can replenish the V^{4+}–O–Ti bonds. A trace amount of ethyl lactate was converted to ethyl pyruvate in nitrogen initially, probably due to the oxygen sill chemisorbed on the surface of VTN. This anaerobic process of lactate-to-pyruvate was also observed by *in situ* DRIFTS experiments at elevated temperatures under helium atmosphere. The V^{4+}–O–Ti bonds were gradually decreased and shifted to higher wavelengths, accompanying the formation of characteristic peaks of pyruvate (Figure S12).

Based on the experimental and computational results, we can propose a probable mechanism (Scheme 2). Starting with the pristine catalyst VTN, ethyl lactate adsorbs and then chemisorbs by the coordinated bond to titanium atoms **a** and further forms the transition state **b**. Then, the hydroxyl H atom transfers to near V^{4+}–O–Ti sites, forming the Ti^{4+}-O-substrate intermediate and a V^{4+}-O-H bond (**c)**. This is followed by β-hydrogen activation through an interaction with an adjacent V^{4+}–O–Ti oxygen, giving the five-membered intermediate **d**. Ethyl pyruvate is then produced by β-hydrogen elimination, giving water as by-product as well as creating an oxygen vacancy (**e, f**). Finally, adsorbed oxygen replenishes the oxygen vacancy, regenerating the V^{4+}–O–Ti bonds. In general, structural defects, containing lower oxidation state cations are reported to be necessary to activate the oxygen. Here, we anticipate that V^{4+}, because of its lower oxidation state, can activate oxygen better than V^{5+}. This could be also connected with the fact that a linear relationship is observed between TOF and the amount of V^{4+} in the samples.

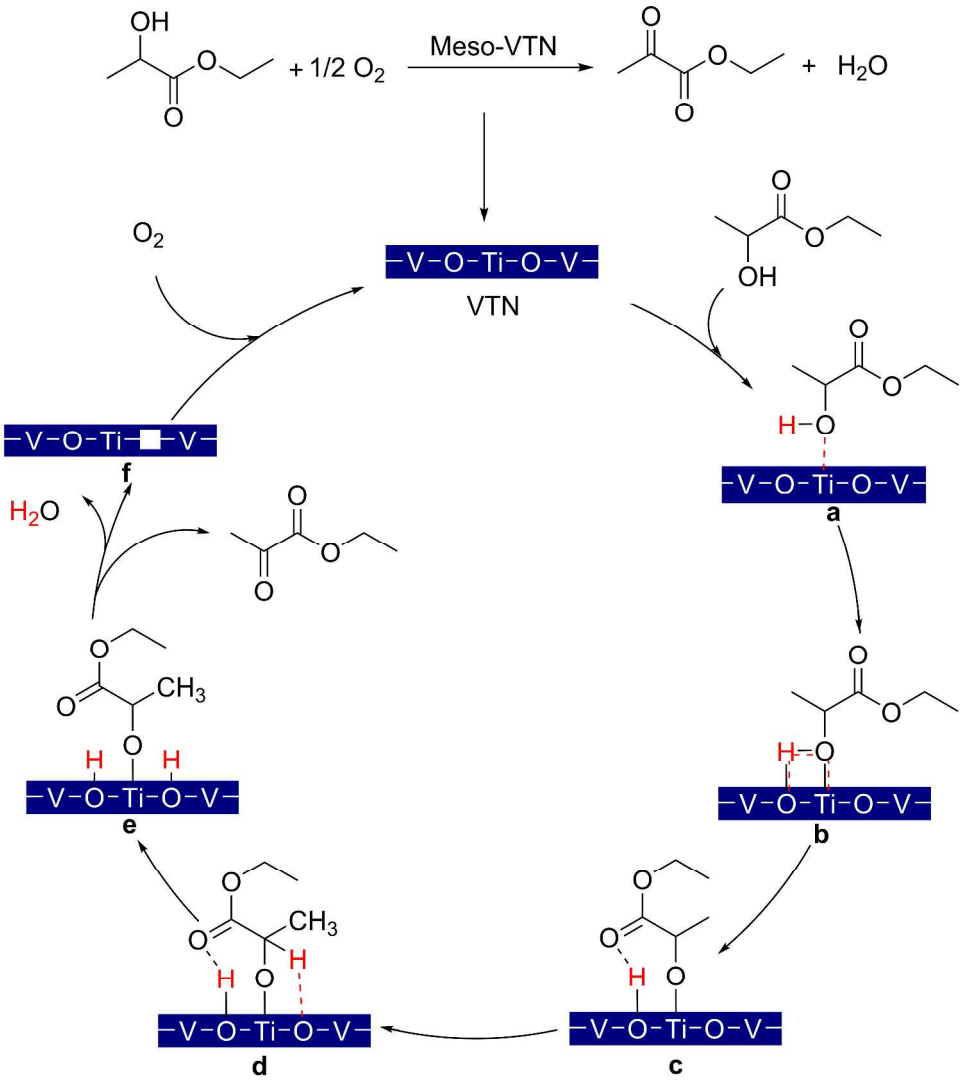

Scheme 2. Proposed catalytic cycle for the oxidative dehydrogenation of ethyl lactate to ethyl pyruvate in the presence of meso-VTN.

CONCLUSIONS

We developed a one-pot strategy for the controllable synthesis of uniform mesoporous vanadia-titania nanoparticles (VTNs). NH_4VO_3 is the optimal vanadium precursor, forming primarily monomeric VO_4 units, avoiding the agglomeration of polymeric vanadium species as well as the formation of rutile structure to a great extent. In comparison to homogeneous vanadium

compounds and classical VO_x-TiO_2 prepared by impregnation, the meso-VTN catalysts showed superior catalytic activity and selectivity for the ODH of ethyl lactate to ethyl pyruvate. In addition, V^{4+} as the major valence state was incorporated into the anatase TiO_2, which can increase the availability of surface chemisorbed oxygen, resulting in high catalytic activity for aerobic oxidation of ethyl lactate. Hot filtration and recyclability tests confirmed that NH_4VO_3@VTN does not leach into solution, and can be reused at least ten times without loss of activity. *In situ* DRIFTS and DFT simulations show that ethyl lactate adsorbs preferentially on the VTN surface via the coordination of hydroxyl oxygen to titanium. The V^{4+}–O–Ti bonds play a key role in the dissociation of ethyl lactate, and further promote the deprotonation of β-hydrogen. In addition, molecular oxygen can replenish the surface oxygen to regenerate the V^{4+}–O–Ti bonds. Thus, this work provides fundamental insights for developing further simple and cost-effective catalytic systems for highly efficient conversion of biomass derivatives to value-added chemicals under mild conditions.

ASSOCIATED CONTENT

Supporting information

The Supporting Information is available free of charge on the ACS Publications website.

Experimental procedures, computational details, additional characterization data of VTN catalysts including XRD patterns, nitrogen adsorption-desorption isotherms, SEM/TEM images, EDX spectra, XPS spectra, H_2-TPR profiles and *in situ* DRIFT spectra. Results on hot filtration tests and the effect of addition of free-radical scavengers.

AUTHOR INFORMATION

Corresponding Authors

*E-mail: n.r.shiju@uva.nl

*E-mail: b.ensing@uva.nl

Notes

There are no conflicts to declare.

ACKNOWLEDGMENT

WZ thanks the China Scholarship Council for a PhD fellowship. This work is part of the Research Priority Area Sustainable Chemistry of the UvA, http://suschem.uva.nl.

REFERENCES

(1) Gallezot, P. *Chem. Soc. Rev.* **2012**, *41*, 1538-1558.

(2) Beerthuis, R.; Rothenberg, G.; Shiju, N. R. *Green Chem.* **2015**, *17*, 1341-1361.

(3) Dusselier, M.; Van Wouwe, P.; Dewaele, A.; Makshina, E.; Sels, B. F. *Energy Environ. Sci.* **2013**, *6*, 1415-1442.

(4) Mäki-Arvela, P.; Simakova, I. L.; Salmi, T.; Murzin, D. Y. *Chem. Rev.* **2014**, *114*, 1909-1971.

(5) Xu, P.; Qiu, J.; Gao, C.; Ma, C. *J. Biosci. Bioeng.* **2008**, *105*, 169-175.

(6) Sousa, S. C. A.; Fernandes, A. C. *Coord. Chem. Rev.* **2015**, *284*, 67-92.

(7) Ai, M. *Appl. Catal. A* **2002**, *232*, 1-6.

(8) Zhao, X.; Zhang, C.; Xu, C.; Li, H.; Huang, H.; Song, L.; Li, X. *Chem. Eng. J.* **2016**, *296*, 217-224.

(9) Liu, K. T.; Huang, X. M.; Pidko, E. A.; Hensen, E. J. M. *Green Chem.* **2017**, *19*, 3014-3022.

(10) Lomate, S.; Bonnotte, T.; Paul, S.; Dumeignil, F.; Katryniok, B. *J. Mol. Catal. A: Chem.* **2013**, *377*, 123-128.

(11) Sugiyama, S.; Kikumoto, T.; Tanaka, H.; Nakagawa, K.; Sotowa, K.-I.; Maehara, K.; Himeno, Y.; Ninomiya, W. *Catal. Lett.* **2009**, *131*, 129-134.

(12) Mallat, T.; Baiker, A. *Chem. Rev.* **2004**, *104*, 3037-3058.

(13) Tsujino, T.; Ohigashi, S.; Sugiyama, S.; Kawashiro, K.; Hayashi, H. *J. Mol. Catal.* **1992**, *71*, 25-35.

(14) Zhang, C.; Wang, T.; Ding, Y. J. *Appl. Catal. A* **2017**, *533*, 59-65.

(15) Wachs, I. E. *Dalton Trans.* **2013**, *42*, 11762-11769.

(16) Yasukawa, T.; Ninomiya, W.; Ooyachi, K.; Aoki, N.; Mae, K. *Chem. Eng. J.* **2011**, *167*, 527-530.

(17) Yasukawa, T.; Ninomiya, W.; Ooyachi, K.; Aoki, N.; Mae, K. *Ind. Eng. Chem. Res.* **2011**, *50*, 3858-3863.

(18) Nguyen, H. G. T.; Schweitzer, N. M.; Chang, C.-Y.; Drake, T. L.; So, M. C.; Stair, P. C.; Farha, O. K.; Hupp, J. T.; Nguyen, S. T. *ACS Catal.* **2014**, *4*, 2496-2500.

(19) Ramos-Fernandez, E. V.; Geels, N. J.; Shiju, N. R.; Rothenberg, G. *Green Chem.* **2014**, *16*, 3358-3363.

(20) Kim, J.; McNamara, N. D.; Hicks, J. C. *Appl. Catal. A* **2016**, *517*, 141-150.

(21) Rothenberg, G.; de Graaf, E. A.; Bliek, A. *Angew. Chem. Int. Ed.* **2003**, *42*, 3366-3368.

(22) Zamani, S.; Meynen, V.; Hanu, A.-M.; Mertens, M.; Popovici, E.; Van Doorslaer, S.; Cool, P. *PCCP* **2009**, *11*, 5823-5832.

(23) Shi, Q.; Li, Y.; Zhan, E.; Ta, N.; Shen, W. *CrystEngComm* **2015**, *17*, 3376-3382.

(24) Choi, J.; Shin, C. B.; Park, T.-J.; Suh, D. J. *Appl. Catal. A* **2006**, *311*, 105-111.

(25) Long, L.-L.; Zhang, A.-Y.; Yang, J.; Zhang, X.; Yu, H.-Q. *ACS Appl. Mater. Interfaces* **2014**, *6*, 16712-16720.

(26) Schimmoeller, B.; Schulz, H.; Ritter, A.; Reitzmann, A.; Kraushaar-Czametzki, B.; Baiker, A.; Pratsinis, S. E. *J. Catal.* **2008**, *256*, 74-83.

(27) Ortel, E.; Sokolov, S.; Zielke, C.; Lauermann, I.; Selve, S.; Weh, K.; Paul, B.; Polte, J.; Kraehnert, R. *Chem. Mater.* **2012**, *24*, 3828-3838.

(28) Sivaranjani, K.; Verma, A.; Gopinath, C. S. *Green Chem.* **2012**, *14*, 461-471.

(29) Yoshitake, H.; Tatsumi, T. *Chem. Mater.* **2003**, *15*, 1695-1702.

(30) Hossain, M. K.; Akhtar, U. S.; Koirala, A. R.; Hwang, I. C.; Yoon, K. B. *Catal. Today* **2015**, *243*, 228-234.

(31) Hanson, S. K.; Wu, R.; Silks, L. A. P. *Org. Lett.* **2011**, *13*, 1908-1911.

(32) Bie, Z.; Li, G.; Wang, L.; Lv, Y.; Niu, J.; Gao, S. *Tetrahedron Lett.* **2016**, *57*, 4935-4938.

(33) Jun, Y.-S.; Park, J.; Lee, S. U.; Thomas, A.; Hong, W. H.; Stucky, G. D. *Angew. Chem. Int. Ed.* **2013**, *125*, 11289-11293.

(34) Yun, D.; Kim, T. Y.; Park, D. S.; Yun, Y. S.; Han, J. W.; Yi, J. *ChemSusChem* **2014**, *7*, 2193-2201.

(35) Khatun, N.; Rini, E. G.; Shirage, P.; Rajput, P.; Jha, S. N.; Sen, S. *Mater. Sci. Semicond. Process.* **2016**, *50*, 7-13.

(36) Zavahir, S.; Xiao, Q.; Sarina, S.; Zhao, J.; Bottle, S.; Wellard, M.; Jia, J.; Jing, L.; Huang, Y.; Blinco, J. P.; Wu, H.; Zhu, H.-Y. *ACS Catal.* **2016**, *6*, 3580-3588.

(37) Feng, S.; Li, W.; Shi, Q.; Li, Y.; Chen, J.; Ling, Y.; Asiri, A. M.; Zhao, D. *Chem. Commun.* **2014**, *50*, 329-331.

(38) Zhang, W.; Wang, Q.; Wu, H.; Wu, P.; He, M. *Green Chem.* **2014**, *16*, 4767-4774.

(39) Zhang, W.; Liu, T.; Wu, H.; Wu, P.; He, M. *Chem. Commun.* **2015**, *51*, 682-684.

(40) Wei, J.; Zhou, D.; Sun, Z.; Deng, Y.; Xia, Y.; Zhao, D. *Adv. Funct. Mater.* **2013**, *23*, 2322-2328.

(41) Zhang, R.; Tu, B.; Zhao, D. *Chem. Eur. J.* **2010**, *16*, 9977-9981.

(42) Avansi, W.; Arenal, R.; de Mendonca, V. R.; Ribeiro, C.; Longo, E. *CrystEngComm* **2014**, *16*, 5021-5027.

(43) Zhang, J.; Li, M.; Feng, Z.; Chen, J.; Li, C. *J. Phys. Chem. B* **2006**, *110*, 927-935.

(44) Su, J.; Zou, X.; Li, G.-D.; Jiang, Y.-M.; Cao, Y.; Zhao, J.; Chen, J.-S. *Chem. Commun.* **2013**, *49*, 8217-8219.

(45) Liu, H.; Wu, Y.; Zhang, J. *ACS Appl. Mater. Interfaces* **2011**, *3*, 1757-1764.

(46) Li, A.; Wang, Z.; Yin, H.; Wang, S.; Yan, P.; Huang, B.; Wang, X.; Li, R.; Zong, X.; Han, H.; Li, C. *Chem. Sci.* **2016**, *7*, 6076-6082.

(47) Pradhan, S.; Bartley, J. K.; Bethell, D.; Carley, A. F.; Conte, M.; Golunski, S.; House, M. P.; Jenkins, R. L.; Lloyd, R.; Hutchings, G. J. *Nat Chem* **2012**, *4*, 134-139.

(48) Gouma, P. I.; Mills, M. J. *J. Am. Ceram. Soc.* **2001**, *84*, 619-622.

(49) Luo, W.; Li, Y.; Dong, J.; Wei, J.; Xu, J.; Deng, Y.; Zhao, D. *Angew. Chem. Int. Ed.* **2013**, *125*, 10699-10704.

(50) Bulushev, D. A.; Rainone, F.; Kiwi-Minsker, L.; Renken, A. *Langmuir* **2001**, *17*, 5276-5282.

(51) Khan, M.; Song, Y. T.; Chen, N.; Cao, W. B. *Mater. Chem. Phys.* **2013**, *142*, 148-153.

(52) Luo, Z.; Poyraz, A. S.; Kuo, C.-H.; Miao, R.; Meng, Y.; Chen, S.-Y.; Jiang, T.; Wenos, C.; Suib, S. L. *Chem. Mater.* **2015**, *27*, 6-17.

(53) Carrero, C. A.; Schloegl, R.; Wachs, I. E.; Schomaecker, R. *ACS Catal.* **2014**, *4*, 3357-3380.

(54) Zhao, W.; Zhong, Q. *RSC Adv.* **2014**, *4*, 5653-5659.

(55) Lee, K. J.; Kumar, P. A.; Maqbool, M. S.; Rao, K. N.; Song, K. H.; Ha, H. P. *Appl. Catal. B* **2013**, *142-143*, 705-717.

(56) Kang, M.; Park, E. D.; Kim, J. M.; Yie, J. E. *Appl. Catal. A* **2007**, *327*, 261-269.

(57) Nakka, L.; Molinari, J. E.; Wachs, I. E. *J. Am. Chem. Soc.* **2009**, *131*, 15544-15554.

(58) Song, H.; Jeong, T. G.; Moon, Y. H.; Chun, H. H.; Chung, K. Y.; Kim, H. S.; Cho, B. W.; Kim, Y. T. *Sci. Rep.* **2014**, *4*, 4350.

(59) Boningari, T.; Somogyvari, A.; Smimiotis, P. G. *Ind. Eng. Chem. Res.* **2017**, *56*, 5483-5494.

(60) Slot, T. K.; Eisenberg, D.; van Noordenne, D.; Jungbacker, P.; Rothenberg, G. *Chem. Eur. J.* **2016**, *22*, 12307-12311.

(61) Chen, Y.-K.; Lin, Y.-F.; Peng, Z.-W.; Lin, J.-L. *J. Phys. Chem. C* **2010**, *114*, 17720-17727.

(62) Cassanas, G.; Morssli, M.; Fabrègue, E.; Bardet, L. *J. Raman Spectrosc.* **1991**, *22*, 409-413.

(63) Kaichev, V. V.; Chesalov, Y. A.; Saraev, A. A.; Klyushin, A. Y.; Knop-Gericke, A.; Andrushkevich, T. V.; Bukhtiyarov, V. I. *J. Catal.* **2016**, *338*, 82-93.

(64) Chieregato, A.; Bandinelli, C.; Concepción, P.; Soriano, M. D.; Puzzo, F.; Basile, F.; Cavani, F.; Nieto, J. M. L. *ChemSusChem* **2017**, *10*, 234-244.

(65) Wen, B.; Li, Y.; Chen, C.; Ma, W.; Zhao, J. *Chem. Eur. J.* **2010**, *16*, 11859-11866.

(66) Garcia, A.; Yan, N.; Vincent, A.; Singh, A.; Hill, J. M.; Chuang, K. T.; Luo, J.-L. *J. Mater. Chem. A* **2015**, *3*, 23973-23980.

(67) Gärtner, C. A.; van Veen, A. C.; Lercher, J. A. *J. Am. Chem. Soc.* **2014**, *136*, 12691-12701.

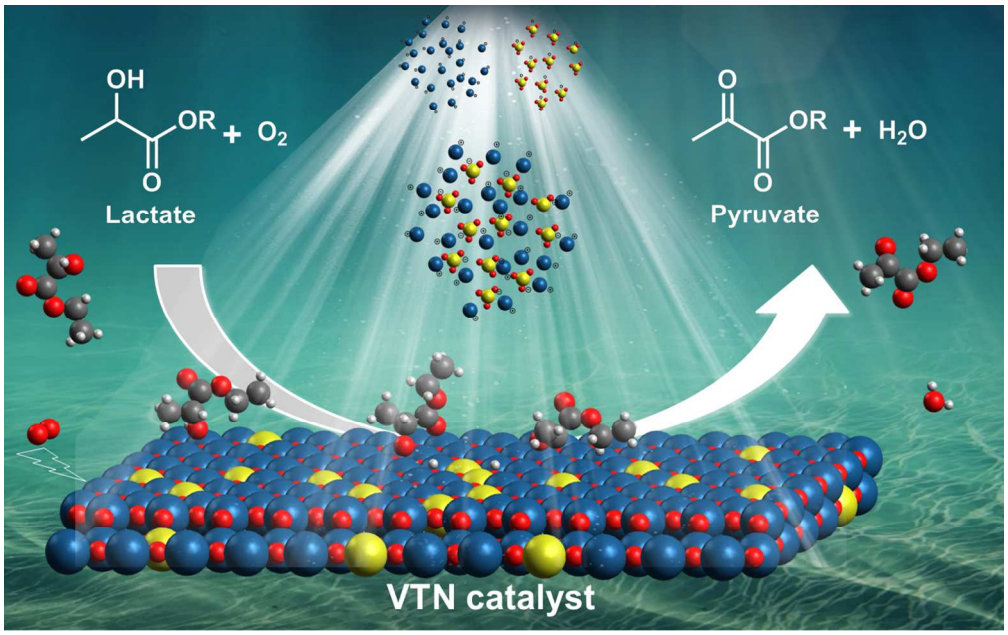

245x152mm (149 x 150 DPI)